Joule

CellPress

Article

Kinetics and mechanism of heterogeneous voltage-driven water-dissociation catalysis

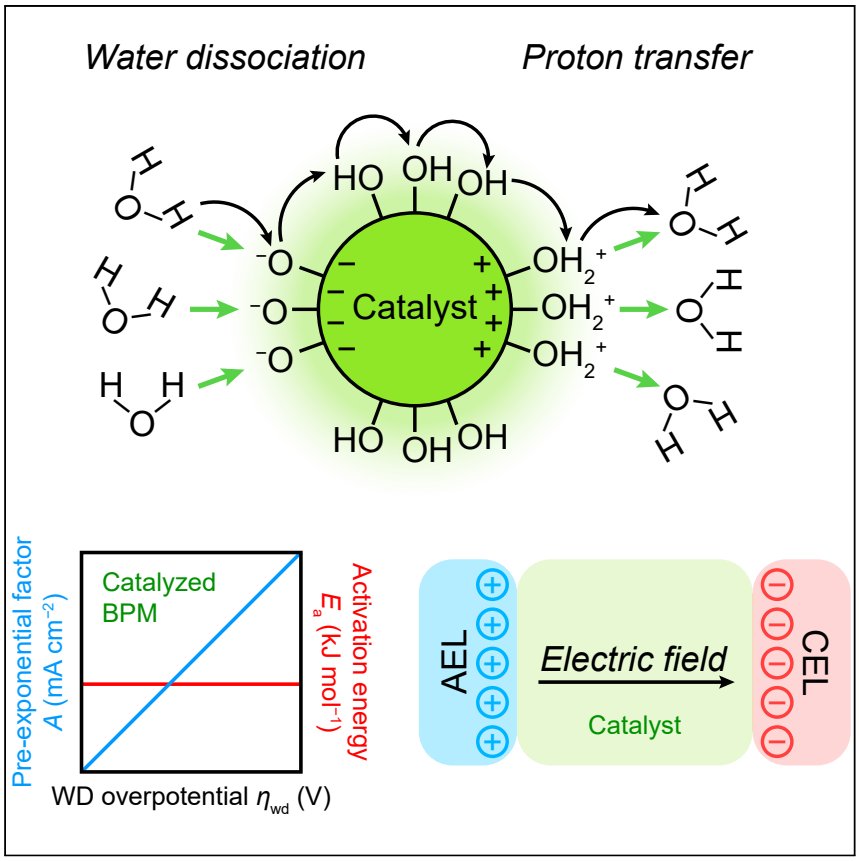

Bipolar membranes (BPMs) are key components of advanced electrodialysis, water electrolysis, CO_2 reduction, and other environmental energy-related fields, but how the applied voltage dissociates water on heterogeneous BPM-junction catalysts is poorly understood, hampering the development of improved designs. We report temperature-dependent water-dissociation kinetics in catalyzed BPMs showing how kinetic parameters depend on water-dissociation-driving force and present a fundamentally new mechanism to explain the results.

Lihaokun Chen, Qiucheng Xu, Shannon W. Boettcher

swb@uoregon.edu

Highlights

Water dissociation (WD) overpotential η_{wd} is accurately measured in bipolar membranes

Arrhenius analysis shows unexpected kinetic parameter dependence on η_{wd}

A new equation is proposed, and physical meanings of parameters are discussed

A new WD mechanism based on proton transfer/transport is proposed

Chen et al., Joule 7, 1–20
August 16, 2023 © 2023 Elsevier Inc.
https://doi.org/10.1016/j.joule.2023.06.011

Please cite this article in press as: Chen et al., Kinetics and mechanism of heterogeneous voltage-driven water-dissociation catalysis, Joule (2023), https://doi.org/10.1016/j.joule.2023.06.011

Joule

CellPress

Article

Kinetics and mechanism of heterogeneous voltage-driven water-dissociation catalysis

Lihaokun Chen,[1] Qiucheng Xu,[1,2] and Shannon W. Boettcher[1,3,*]

SUMMARY

The water-dissociation (WD) reaction ($H_2O \rightarrow H^+ + OH^-$) affects the rates of electrocatalytic reactions and the performance of bipolar membranes (BPMs), but how WD is driven by voltage and catalyzed is not understood. We report BPM electrolyzers with two reference electrodes (REs) to measure temperature-dependent WD current and overpotential (η_{wd}) without soluble electrolyte. Using TiO_2-P25-nanoparticle catalyst and Arrhenius-type analysis, we found $E_{a,wd}$ of 25–30 kJ/mol, independent of η_{wd}, and a pre-exponential factor proportional to η_{wd} that decreases ~10-fold in D_2O. We propose a new WD mechanism where metal-oxide nanoparticles, polarized by the BPM-junction voltage, serve as proton (1) acceptors (from water) on the negatively charged side of the particle to generate free OH^-, (2) donors on the positively charged side to generate H_3O^+, and (3) surface proton conductors that connect spatially separate donor/acceptor sites. Increasing electric field with η_{wd} orients water for proton transfer, increasing the pre-exponential factor, but is insufficient to lower E_a.

INTRODUCTION

When water is consumed as a reactant in chemical and (electro)catalytic processes, water dissociation (WD, $H_2O \rightarrow H^+ + OH^-$) is often a critical elementary step. In a bipolar membrane (BPM), for example, water is dissociated at the junction between an ionomer anion-exchange layer (AEL) and a cation-exchange layer (CEL), usually accelerated by a catalyst sandwiched between the two and driven by an applied voltage (Figure 1A).[1–5] This catalyzed, voltage-driven WD process is not understood, even though BPMs are used in electrodialysis to produce acid/base from brine and to desalinate water,[6–9] in food processing to adjust pH,[10] and in a variety of recycling and separations processes.[11] BPMs can also couple different pH microenvironments, leading to novel uses in fuel cells,[12,13] flow batteries,[14] and water[15,16] and CO_2 electrolyzers[17,18] that can be impurity-tolerant[19] and enable the use of efficient and abundant electrocatalysts. Elementary reaction steps similar to WD are also likely key in electrocatalytic reactions including hydrogen evolution and CO_2 reduction that require protons in neutral-to-basic media where water is the only available proton donor. These analogous proton-transfer processes may also be voltage-driven in the electrochemical double layer and accelerated via surface reactions.[15,20–22]

The efficiency of WD is central to the performance of BPMs. We recently showed that metal-oxide nanoparticles dramatically accelerate the WD reaction both in BPMs and as a step in electrocatalysis[15] and that the ability of the WD catalyst to screen and focus the interfacial electric field in the BPM junction is important.[23] Previously, either an electric field effect (the so-called second Wien effect),[24–27] a catalytic effect,[15,28,29] or a combination of two[23,30,31] has been invoked to explain WD kinetics in the BPM

CONTEXT & SCALE

Water dissociation (WD, $H_2O \rightarrow H^+ + OH^-$) is one of the most important reactions in chemistry. The rate of WD controls the performance of bipolar membranes (BPMs), which can convert electrical energy into acid and base solutions for water treatment or for direct air- or ocean-based CO_2 capture, and electrocatalysis reactions that are central to renewable electrical energy storage such as the reduction of water to H_2 and of CO_2 to fuels. We report a new method to accurately measure the voltage required to drive WD as a function of temperature using a BPM-water-electrolyzer platform and we illustrate a fundamentally new model for how the WD reaction can be catalyzed by nanoparticle surfaces able to donate, accept, and transport protons on their surfaces.

Please cite this article in press as: Chen et al., Kinetics and mechanism of heterogeneous voltage-driven water-dissociation catalysis, Joule (2023), https://doi.org/10.1016/j.joule.2023.06.011

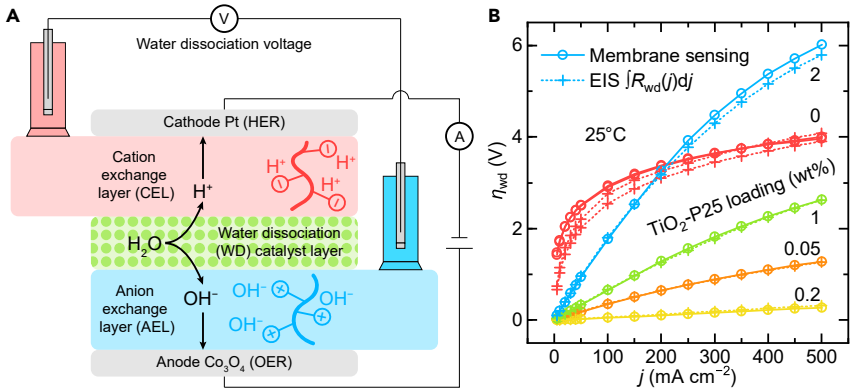

Figure 1. Schematic of membrane-potential sensing in a bipolar membrane (BPM) electrolyzer and comparison with electrochemical-impedance-spectroscopy (EIS) measurements

(A) In the AEL, positive functional groups (e.g., quaternary ammonium cations) are fixed to the polymer backbone while small anions like OH^- are mobile. In the CEL, negative groups (e.g., sulfonate) are fixed to the polymer backbone and small cations like H^+ are mobile. Pure water is fed to cathode and anode gas-diffusion electrodes and diffuses into the BPM. WD occurs at the junction of the AEL and CEL. The voltage between the two reference electrodes connected to the AEL and CEL by membrane strips is recorded as a function of applied current. By subtracting the values at open circuit, the WD overpotential η_{wd} is calculated.

(B) The impedance spectra from the entire cell were measured at different current densities j. The WD resistances R_{wd} were extracted by fitting the spectra and η_{wd} was calculated by integrating R_{wd} as a function of j. Loading is represented by the spin-coat ink concentration; 0.2 wt% yields ~10 μg cm^{-2} or ~200-nm-thick nanoparticle films.

orders of magnitude faster than the equilibrium rates in bulk water, but how the field and catalysis interact at the microscopic/mechanistic level is largely unknown.

These previous studies are also limited in how they assess the WD voltage, usually in H-cells or multi-compartment cells with supporting electrolytes that contain salt ions (other than H^+ and OH^-) such as Na^+ and Cl^-. The current carried by salt ions complicates the analysis of the polarization curves and the study of WD with unknown contributions from series resistance. Temperature-dependent kinetics are central to understanding mechanisms and extracting activation energies (E_a), but these are rarely done for BPMs due to the experimental difficulties in isolating the WD overpotential (i.e., the thermodynamic driving force for WD)[15] from other temperature-dependent processes. The few previous studies have found widely ranging apparent activation energies from ~10 to 80 kJ mol^{-1}, primarily measured for commercial BPMs where the interface chemistry and structure where WD occurs are unknown.[28,32–35] The WD rate constant also depends on the pre-exponential factor (or frequency factor) A, which is seldom discussed in the above, as is unfortunately typical in electrochemistry, despite its importance.[36–39]

We previously avoided these complications by using BPMs in a pure-water electrolyzer, without salt ions, where H^+ and OH^- are the only ionic charge carriers.[15,40] We also demonstrated that the (areal) WD resistance R_{wd} can be isolated from the total impedance (that includes electrode reaction and transport) via electrochemical impedance spectroscopy (EIS).[23] The WD overpotential/overvoltage η_{wd} is calculated from R_{wd} by

$$\eta_{wd} = \int_0^j R_{wd}(j)\,dj \qquad \text{(Equation 1)}$$

[1]Department of Chemistry and the Oregon Center for Electrochemistry, University of Oregon, Eugene, OR 97403, USA

[2]Present address: Surface Physics and Catalysis (Surf Cat) Section, Department of Physics, Technical University of Denmark, 2800 Kgs. Lyngby, Denmark

[3]Lead contact

*Correspondence: swb@uoregon.edu

https://doi.org/10.1016/j.joule.2023.06.011

Please cite this article in press as: Chen et al., Kinetics and mechanism of heterogeneous voltage-driven water-dissociation catalysis, Joule (2023), https://doi.org/10.1016/j.joule.2023.06.011

where j is the current density. R_{wd} is a differential resistance that is a function of j (or equivalently, η_{wd}, the driving force for WD). R_{wd} decreases with driving force and thus j. When R_{wd} does not depend on j, Equation 1 reduces to Ohm's law. Estimating η_{wd} in this way requires measuring EIS at different j, which is slow due to the need for low-frequency data. Some BPMs also degrade during prolonged testing, making it difficult to separate temperature-dependent kinetics from other processes because degradation will underestimate E_a in a temperature step-up experiment but overestimate E_a in a temperature step-down experiment. In Nyquist plots, the WD semicircle is sometimes not well-separated, and low-frequency inductive loops can appear, complicating the analysis and introducing error.

Here, we report a "membrane-potential sensing" method to directly measure η_{wd} in BPM electrolyzers as a function of temperature and current and use it to discover new underlying physical processes controlling WD rates. We used a simpler setup in anion-exchange-membrane electrolyzers to separate the anode and cathode voltage with one reference electrode (RE),[41] as also reported earlier for fuel cells.[42–44] An AEL and a CEL membrane-sensing strip are connected to the AEL and CEL of the BPM, respectively (Figure 1A), with separate REs attached to each strip. After subtracting the open-circuit values, η_{wd} is the voltage between the two references (the ohmic drop across AEL and CEL is small and can be ignored, see more discussion in the experimental procedures). We demonstrate that η_{wd} measured by membrane-potential sensing is almost identical to that from EIS, corroborating both approaches. We use the method to study temperature-dependent WD kinetics on model TiO_2-P25 catalyst. We discover that uncatalyzed BPMs show decreasing E_a with driving force, as expected from typical electrode-kinetics models such as the Butler-Volmer model. In contrast, WD in catalyzed BPMs has an apparent E_a that is almost independent of η_{wd}, but a pre-exponential factor A that surprisingly increases linearly with η_{wd}. We develop a semi-empirical "BPM equation" to quantitatively describe the temperature-dependent kinetics based on the equilibrium activation energy $E_{a,0}$, the effective proton-transfer coefficient α (to describe the effect of η_{wd} on the activation barrier), and a pre-exponential factor A that depends linearly on η_{wd}. Kinetic-isotope experiments show that BPMs fed D_2O have higher η_{wd} than H_2O, with similar E_a and different A. Adding electronically conducting acetylene carbon black (ACB) to a thick layer of TiO_2-P25 both lowers E_a and increases the sensitivity of E_a on η_{wd}, supporting the hypothesis that the electric field is concentrated by conductors to increase WD kinetics. With these data, we then elaborate a new mechanism of field/voltage-driven WD catalysis that includes field-dependent organization of surface water that facilitates proton transfer between near-surface water and the (polarized) metal-oxide WD catalyst, and proton transport across the nanoparticle catalyst surface.

RESULTS AND DISCUSSION

Comparison between membrane-potential-sensing and EIS methods

Previously, we showed that EIS can be used to isolate the WD resistance R_{wd} from the total-cell impedance (Figure S1).[23] In a Nyquist plot, the high-frequency semicircle is related to WD, whereas the low-frequency semicircles are related to anode and cathode charge-transfer resistances and capacitances. Equivalent-circuit fits are used to extract R_{wd} for each different j. Integrating R_{wd} as a function of j, we calculate $\eta_{wd} = \int_0^j R_{wd}(j)\mathrm{d}j$. To corroborate the membrane-potential-sensing and EIS methods, we compare the two ways to calculate η_{wd} for the same sample (Figure 1B). The methods produce similar η_{wd}-j curves, regardless of WD catalyst loadings. Because the EIS measurement is slow, making degradation effects more serious

Please cite this article in press as: Chen et al., Kinetics and mechanism of heterogeneous voltage-driven water-dissociation catalysis, Joule (2023), https://doi.org/10.1016/j.joule.2023.06.011

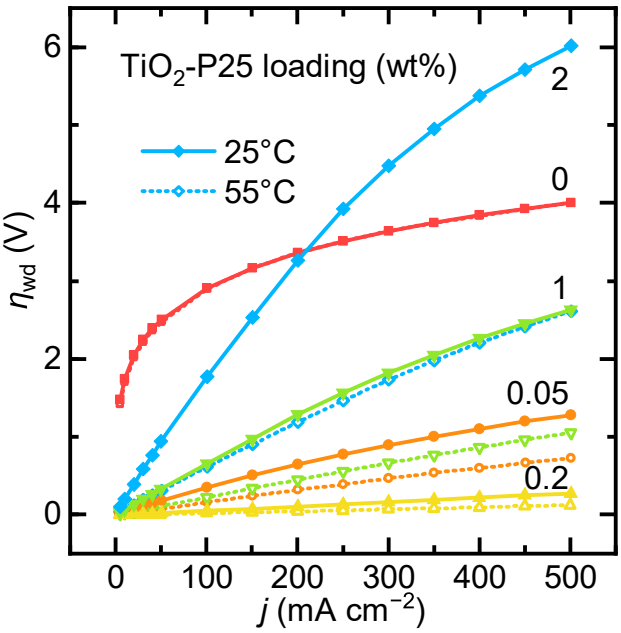

Figure 2. Temperature-dependent polarization curves of BPMs with different mass loadings of TiO_2-P25 WD catalyst

The j-η_{wd} response changes from exponential to linear, and then to a combination of linear and exponential with increasing loading. Temperatures tested were 25°C, 35°C, 45°C, and 55°C ± 2°C, but only data at 25°C and 55°C are shown here for clarity. The uncatalyzed BPM (labeled 0) has almost no apparent temperature dependence at the high current densities tested here due to concomitant degradation processes.

See also Figure S2.

and complicating the temperature-dependence measurement, we use the data from membrane-potential sensing in the analysis below.

Temperature dependence and Arrhenius analysis

The WD polarization curves with different TiO_2-P25 loadings from 25°C to 55°C are shown in Figures 2 and S2. We chose TiO_2-P25 as the model catalyst due to its abundance, low cost, and good performance as a single-composition catalyst in BPM electrolyzers. The optimal loading is 0.2 wt% (represented by the spin-coat ink concentration; equivalent to ~10 μg cm^{-2} and ~200 nm in thickness).[23] Seven loadings were tested and, as expected, when the WD catalyst loading decreases, the polarization curves converge to the pristine BPM without WD catalyst (Figure S3). In pristine BPMs without WD catalyst, j increases exponentially with η_{wd}, like a typical electrochemical reaction with Tafel-like behavior (or Marcus/Butler-Volmer behavior, which are fundamentally related). In contrast, BPMs with an optimal loading of TiO_2-P25 show a linear dependence of j on η_{wd}, more like a resistor that follows Ohm's law. Polarization curves of BPMs with other loadings lie between these two cases, i.e., with a (nearly) linear shape when η_{wd} is small and more exponential when η_{wd} is large. The linear relationship is analogous to the limiting case of the Butler-Volmer model when the exchange current density j_0 is large, or in other words, the electrode charge-transfer kinetics are fast and only a small overpotential η is needed to drive a large current density (see discussion below).

Increasing the temperature lowers η_{wd} in most cases, except for the BPM without catalyst. This artifact was because the pristine uncatalyzed BPM performance

Please cite this article in press as: Chen et al., Kinetics and mechanism of heterogeneous voltage-driven water-dissociation catalysis, Joule (2023), https://doi.org/10.1016/j.joule.2023.06.011

degrades during testing, obscuring the temperature dependence. The reason that pristine, uncatalyzed BPMs degrade so fast is yet unclear but could be due to chemical degradation of the fixed-charge groups on the ionomer at the sharp BPM interface in the presence of the strong electrochemical potential gradient over the abrupt interface under bias or due to current-driven ionomer intermixing. Further studies that combine various spectroscopy techniques are needed to elucidate these mechanisms of uncatalyzed BPM degradation (the optimized catalyzed BPMs have stable WD performance). Therefore, for pristine BPM data reported below, we use only low current densities and a small correction for the calibrated degradation rate (Figure S4). To analyze the data from BPMs with and without WD catalysts, we use an Arrhenius-type model

$$j = Ae^{-\frac{E_a}{RT}} \quad \text{(Equation 2)}$$

where A is the pre-exponential factor, E_a is the apparent activation energy, R is the gas constant, and T is the temperature. Notice that A has the same unit as j (mA cm^{-2}). Since the concentration of the reactant, i.e., water, is unknown inside the BPM junction, we did not normalize A to unit concentration.[36] We assume that the concentration of water is largely constant as we apply $\lesssim$500 mA cm^{-2}, significantly above which water transport into the BPM can be limiting.[40] This assumption is justified because the differential resistance of the polarization curves usually increases when the water transport is limited, as observed at >700 mA cm^{-2} for similar systems previously.[40] Here, the differential resistance decreases or remains constant as j increases (Figure 2).

Our aim was to analyze E_a and A at a fixed η_{wd} (but not j) because η_{wd} represents the driving force, whereas j represents the WD reaction rate. There are no salt ions to otherwise carry current; hence, all measured current must be associated with WD. Because we collect data under current control, the j-η_{wd} data are interpolated with cubic splines (Figure 3A) to generate the Arrhenius plots (ln j plotted against 1/T) at a constant driving force (η_{wd}). We choose cubic splines to capture the curvature of the polarization curves.

For a fixed η_{wd}, the Arrhenius-plot slope and vertical intercept from linear fitting yield E_a and A, respectively. The procedure is repeated for different η_{wd} (Figure 3B) to understand how the driving force for WD modulates kinetics and possible mechanisms. The slope does not change with 1/T (within the temperature range of the experiment); E_a and A are thus independent of T. In the next section, we discuss how E_a and A depend on η_{wd} and WD-catalyst loading, as this informs the microscopic picture of catalyzed WD reactions in BPMs, and more broadly in electrocatalysis where reactions also take place in the presence of a large interfacial electric field.[21,45,46]

Overpotential and mass-loading dependence of kinetic parameters

The apparent E_a and A as a function of η_{wd} with different TiO_2-P25 loadings are shown in Figure 3C. For the pristine BPM without WD catalyst, E_a decreases from 34 to 24 kJ mol^{-1} as η_{wd} increases from 0.2 to 1 V. This behavior is like those observed for interfacial faradaic processes, where the activation energy for electron transfer (e.g., in the Butler-Volmer or Marcus models) is lowered with increasing absolute overpotential. For BPMs with TiO_2-P25 catalyst, however, E_a is essentially constant with η_{wd}. The similar independence of E_a on transmembrane voltage has also been observed occasionally in other studies of BPMs, as mentioned above.[28,34]

Differences in WD processes in BPMs compared with WD in pure water are also apparent (Table 1). In pure water, Eigen and de Maeyer determined the apparent

Please cite this article in press as: Chen et al., Kinetics and mechanism of heterogeneous voltage-driven water-dissociation catalysis, Joule (2023), https://doi.org/10.1016/j.joule.2023.06.011

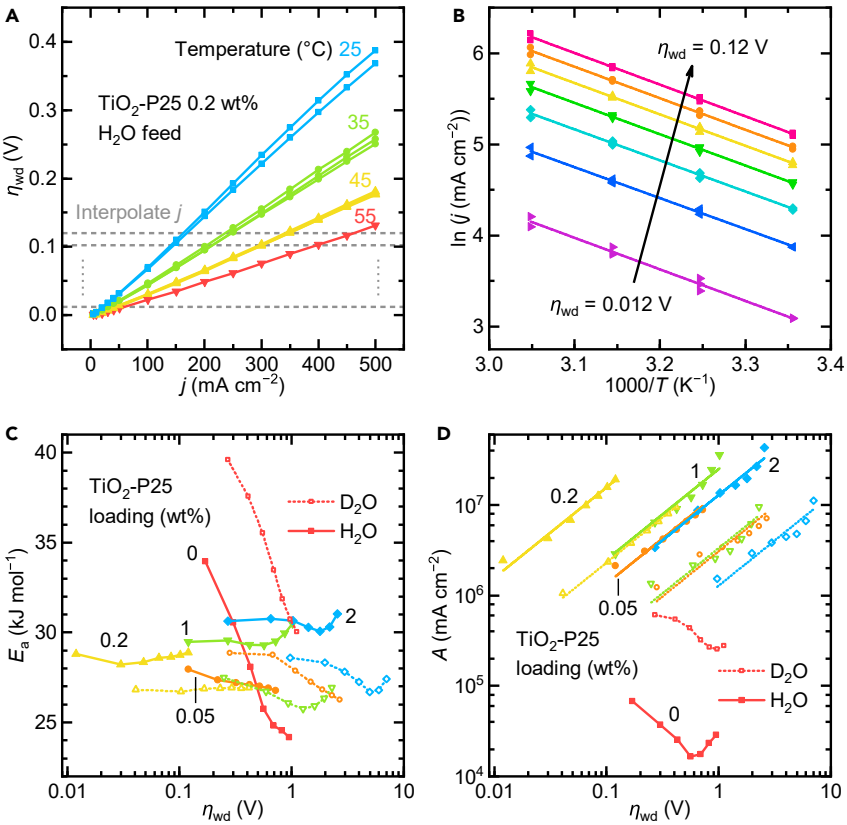

Figure 3. Arrhenius analysis of temperature-dependent BPM polarization curves

(A) Temperature-dependent polarization curves of a BPM with 0.2 wt% TiO_2-P25 and fed by H_2O. The same sample is cycled between 25°C and 55°C. Current density j is interpolated at certain η_{wd}.

(B) Arrhenius plots of a BPM with 0.2 wt% TiO_2-P25 and fed by H_2O at different η_{wd}'s. Lines are least-squares linear fits of the experimental data.

(C) Apparent activation energy E_a as a function of η_{wd}. Different loadings of TiO_2-P25 are used as WD catalyst. The electrolyzer is fed by either H_2O or D_2O. Notice the log scale on the horizontal axis.

(D) The pre-exponential factor A as a function of η_{wd}. Notice the log scale on both axes. Lines are least-squares linear fits with fixed slope of one except the loading of 0. Voltage increases the pre-exponential factor for catalyzed samples instead of lowering the activation barrier.

E_a for WD $E_a(k_D)$ = 64.9–69.0 kJ mol^{-1}, whereas for recombination/neutralization, $E_a(k_R)$ = 8–13 kJ mol^{-1}, where k_D and k_R denote the rate constants of WD and H^+/OH^- recombination/neutralization, respectively.[47,51] Natzle and Moore found $E_a(k_R)$ = 15 $\pm$ 3 kJ mol^{-1}.[49] Since $E_a(k_D)$ and $E_a(k_R)$ are related by the standard enthalpy of WD as $\Delta H^\circ = E_a(k_D) - E_a(k_R)$ = 56 kJ mol^{-1},[50,52] and thus, $E_a(k_D)$ = 71 $\pm$ 3 kJ mol^{-1}, which is comparable with the results of Eigen and de Maeyer. Interestingly, the E_a for WD in BPMs is lower than $E_a(k_D)$ in pure water by a factor of two, suggesting a different mechanism and/or solvation environment.

Unexpectedly, we find that the pre-exponential factor A increases almost linearly with η_{wd} for catalyzed BPMs (Figure 3D, notice the log-log scale and the unit-slope lines), in contrast with classic Butler-Volmer models where E_a decreases linearly with η, and A is independent of η.[36] The Butler-Volmer model, of course, was developed for *electron*-transfer electrode reactions, whereas WD is a *proton*-transfer reaction. However, both involve interfacial *charge* transfer driven by electrochemical potential

Please cite this article in press as: Chen et al., Kinetics and mechanism of heterogeneous voltage-driven water-dissociation catalysis, Joule (2023), https://doi.org/10.1016/j.joule.2023.06.011

Table 1. Kinetic and thermodynamic parameters of H_2O and D_2O dissociation

	H_2O	D_2O	H/D
Dissociation rate constant k_D (10^{-5} s^{-1})	2.5[47]; 2.56[48]; 2.04[49]	0.25[48]; 0.186[49]	~11
Apparent activation energy $E_a(k_D)$ (kJ mol^{-1})	64.9–69.0[47]	76[a48]	~0.88
Neutralization rate constant k_R (10^{11} M^{-1} s^{-1})	1.4[47]; 1.43[48]; 1.12[49]	0.84[48]; 0.741[49]	~1.7
Apparent activation energy $E_a(k_R)$ (kJ mol^{-1})	8–13[47]; 15[49]	15[a48]	~0.85
Dissociation constant K_w (10^{-14})	1.0[50]	0.11[50]	~9.1
Standard Gibbs free energy ΔG° (kJ mol^{-1})	79.87[50]	85.23[50]	~0.94
Standard enthalpy ΔH° (kJ mol^{-1})	55.82[50]	60.87[50]	~0.92
Standard entropy ΔS° (J mol^{-1} K^{-1})	−80.67[50]	−81.75[50]	~0.97

[a]Extracted from Arrhenius analysis using the literature values.

gradients. We use the Butler-Volmer equation as a well-known model to compare with and discuss a microscopic physical picture below.

The BPM equation

The above Arrhenius analysis (based on interpolation and linear fitting) is limited by the η_{wd} of the highest test temperature (e.g., 0.12 V in Figure 3A), as above that there are only data for three temperatures or fewer. We thus developed a semi-empirical equation to fit all the data and minimize the errors due to interpolation. We hypothesize, following the Butler-Volmer model, that

$$E_a = E_{a,0} - \alpha F \eta_{wd} \quad \text{(Equation 3)}$$

where $E_{a,0}$ is the "equilibrium activation energy" and $\alpha \geq 0$ is the "proton-transfer coefficient," a unitless number that describes how E_a for proton transfer changes with η_{wd} and determines the shape of the polarization curve. An α tending to 0 results in a linear j-η_{wd} response (e.g., with optimal TiO_2-P25 loading), whereas a larger α leads to an exponential shape (e.g., as for the pristine BPMs). Because the prefactor A is proportional to η_{wd}, we have

$$A = G_0 \eta_{wd} \quad \text{(Equation 4)}$$

where the new constant $G_0 = A/\eta_{wd}$ has the unit of areal conductance (mS cm^{-2}). Note that the pre-exponential factor A is proportional to η_{wd}, but G_0 itself is independent of η_{wd}. Substituting these relations into the Arrhenius equation yields a semi-empirical BPM equation to describe WD in BPMs (the forward and reverse reaction contributions are not separated explicitly, see more discussion below)

$$j_{wd} = G_0 \eta_{wd} e^{-\frac{E_{a,0} - \alpha F \eta_{wd}}{RT}} = \left(G_0 e^{-\frac{E_{a,0}}{RT}}\right) \eta_{wd} e^{\frac{\alpha F \eta_{wd}}{RT}} \quad \text{(Equation 5)}$$

where G_0, $E_{a,0}$, and α depend on catalyst type and loading. By fitting j as a function of η_{wd} at different T, we extract the parameters G_0, $E_{a,0}$, and α using the entire dataset (Figure 4). For most polarization curves, the fitting provides $R^2 > 0.99$, and the parameter-fitting errors are usually less than 10% of the parameter values (Figure S2). The fit requires variable-temperature polarization curves, since at a fixed T and with fixed catalyst and loading, G_0 and $E_{a,0}$ are interdependent and lumped into the term as $G_0 e^{-\frac{E_{a,0}}{RT}}$. At small η_{wd}, $e^{\frac{\alpha F \eta_{wd}}{RT}} \rightarrow 1$, and the linearized BPM equation is

$$j_{wd} = \left(G_0 e^{-\frac{E_{a,0}}{RT}}\right) \eta_{wd} \quad \text{(Equation 6)}$$

The classical linearized Butler-Volmer equation at small overpotential η provides

$$j_{BV} = \left(\frac{j_{0,BV} F}{RT}\right) \eta \quad \text{(Equation 7)}$$

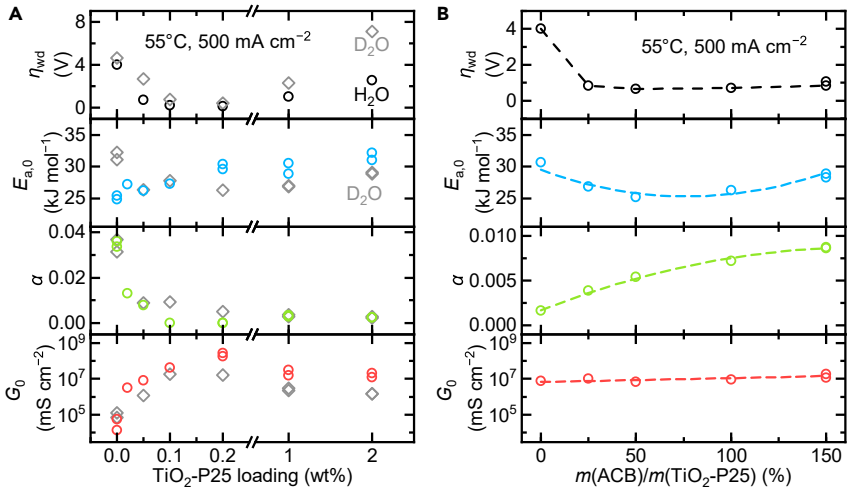

Figure 4. Temperature-dependence analysis using a semi-empirical BPM equation

The current response of a BPM can be expressed as $j_{wd} = G_0\eta_{wd}e^{-\frac{E_{a,0}-\alpha F\eta_{wd}}{RT}}$, where $E_{a,0}$ is the equilibrium activation energy, α is the proton-transfer coefficient, and G_0 is the proton-transfer conductance. To compare with BPM performance, η_{wd} at 55°C and 500 mA cm^{-2} are also included. Notice the log scale on the vertical axis for G_0.

(A) Different loadings of TiO_2-P25 are used as WD catalyst. The electrolyzer is fed by either H_2O or D_2O. Notice the log scale on the horizontal axis.

(B) Different mass ratios of acetylene carbon black (ACB) and TiO_2-P25 are used as WD catalyst. The mass of TiO_2-P25 is kept constant while the mass of ACB is varied. The electrolyzer is fed by H_2O. The increase of the proton-transfer coefficient α with conductive additive is consistent with electric-field screening and focusing. Lines serve as a guide for the eye.

In analogy with Equation 6, we can define a WD exchange current density j_0

$$j_{0,wd} = \frac{RT}{F}G_0e^{-\frac{E_{a,0}}{RT}} \qquad \text{(Equation 8)}$$

Higher G_0 and lower $E_{a,0}$ give a larger j_0, and j_0 increases with temperature. The parameter G_0 can be called the driving-force-independent "proton-transfer conductance" and is likely related to the number of active proton acceptor/donor sites on the WD catalyst surface and the frequency by which water molecules interact with those sites to accommodate proton transfer (see below).

The parameters G_0, $E_{a,0}$, and α depend on TiO_2-P25 loading. $E_{a,0}$ increases from ~25 to ~30 kJ mol^{-1} for the BPM without catalyst to one with optimal loading (0.2 wt%, ~10 μg cm^{-2}, and ~200 nm) then increases slowly and approaches $E_{a,0}$ ~ 32 kJ mol^{-1} when the loading is higher than 1 wt% (Figure 4A). The shape of the polarization curve is related to α (compare Figures 2 and 4A). A smaller α results in a linear j-η_{wd} response, as in the case for optimal loading (α = 0), whereas a larger α yields a more-exponential dependence, as in the very low loadings and without catalyst. Interestingly, G_0 increases substantially with TiO_2-P25 loading before the optimal value (notice the log scale) and then slightly decreases. Lower $E_{a,0}$, higher α, and higher G_0 lead to better performance. In the case of TiO_2-P25, G_0 appears to be the dominant factor and is correlated with η_{wd} (Figure 4A, top and bottom).

Kinetic isotope effects

To obtain information on the rate-limiting step in WD, we fed the BPM electrolyzer with D_2O and measured kinetic-isotopic effects (Figure S5). For the catalyzed BPMs, η_{wd} in

Please cite this article in press as: Chen et al., Kinetics and mechanism of heterogeneous voltage-driven water-dissociation catalysis, Joule (2023), https://doi.org/10.1016/j.joule.2023.06.011

Table 2. Diffusion coefficients and associated activation energies for H_2O, D_2O, and their ions

	H_2O	D_2O	H/D
Diffusion coefficient D (10^{-5} cm^2 s^{-1})	2.299[54]	1.872[54]	~1.2
Apparent activation energy $E_a(D)$ (kJ mol^{-1})	18–20[54]	19–21[54]	~0.95
	H^+	D^+	H/D
Diffusion coefficient D (10^{-5} cm^2 s^{-1})	9.311[55]	6.655[55]	~1.4
Apparent activation energy $E_a(D)$ (kJ mol^{-1})	10.6[56]; 10.0[a57]	10.0[a57]	~1
	OH^-	OD^-	H/D
Diffusion coefficient D (10^{-5} cm^2 s^{-1})	5.273[55]	3.169[55]	~1.7
Apparent activation energy $E_a(D)$ (kJ mol^{-1})	13[56]; 12.6[a57]	13.0[a57]	~1

[a]Activation energy of ionic conductivity is used due to the lack of data.

D_2O is ~2–4 larger than in H_2O (Figure 4A, top) despite both $E_{a,0}$ and α being relatively similar. The larger η_{wd} in D_2O is largely due to a lower G_0 (and thus A), which is evident in Figure 3D. For pristine BPMs, D_2O has a higher E_a than H_2O, whereas catalyzed BPMs have E_a similar or smaller for D_2O compared with H_2O (Figure 3C). In the pristine BPMs, WD likely occurs more like in bulk water, i.e., proton transfer between water molecules under the strong electric field. The H/D ratio of E_a is ~0.8, comparable with the $E_a(k_D)$ for bulk water ~0.88 (Table 1). For catalyzed BPMs, WD occurs on the catalyst surface, and the D_2O-related species might have a lower binding energy to the catalyst surface compared with H_2O, similar to the inverse kinetic isotope effect in the oxygen-reduction reaction.[53] These isotope effects can be compared with those found for diffusion coefficients and associated activation energies for H_2O, D_2O, and their ions (Table 2). Diffusion of these species follows an Arrhenius model with an activation energy of $E_a(D)$. Although the diffusion coefficients show H/D ratios (defined as the value of H species relative to D species, such as H_2O/D_2O, H^+/D^+, and OH^-/OD^-) ranging from 1.2 to 1.7, the H/D ratios of $E_a(D)$ are close to unity. Bulk H_2O and D_2O also show differences in dissociation kinetics (Table 1). Compared with D_2O, the dissociation equilibrium constant K_w and dissociation rate constant k_D of H_2O are 9 and 11 times larger, respectively, whereas both $E_a(k_D)$ are similar. These data are consistent with our experimental results of H_2O and D_2O in voltage-driven catalyzed WD reaction in the BPM; the rates/current densities are substantially slower for D_2O (characterized by A or G_0), but the temperature dependence (characterized by E_a) is similar. These data point to the pre-exponential factor A being associated not only with the number of catalyst proton acceptor/donor sites on the surface but also with the facility by which water molecules can organize via molecular motion for the charge-transfer step, as discussed below.

Effect of electronic conductivity

We previously showed that adding electronic conductors such as ACB nanoparticles to a thick layer (~120 μg cm^{-2} and ~2.4 μm) of TiO_2-P25 WD catalyst improves the BPM performance substantially, likely through focusing the electric at the AEL|catalyst and catalyst|CEL interfaces.[23] We measured the temperature dependence of these thick TiO_2-P25 WD layers mixed with different ratios of ACB (by mass) as WD catalyst. Adding ACB lowered η_{wd} (the optimal ratio is between 50% and 100%), consistent with previous results[23] (Figure 4B). Analysis of the new temperature-dependent data shows that adding ACB lowers $E_{a,0}$ from ~30 to ~26 kJ mol^{-1}, when the mass ratio increases from 0% to 50%, and increases α by a factor

Please cite this article in press as: Chen et al., Kinetics and mechanism of heterogeneous voltage-driven water-dissociation catalysis, Joule (2023), https://doi.org/10.1016/j.joule.2023.06.011

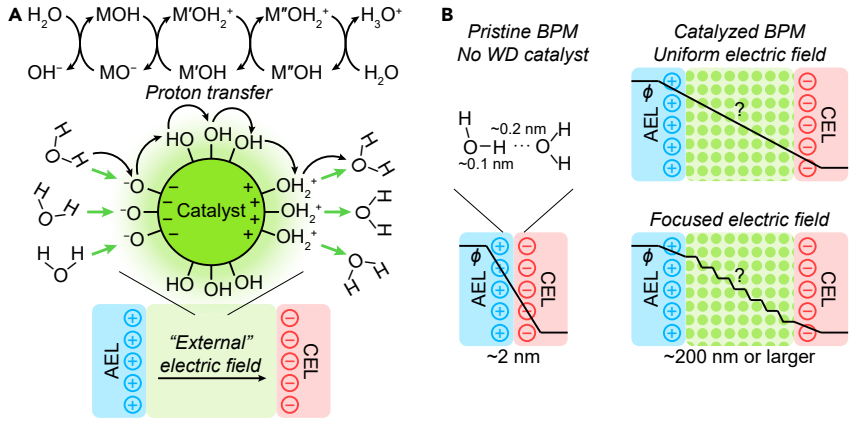

Figure 5. Proposed mechanism for voltage-driven catalyzed WD

(A) The "external" electric field originates from the unbalanced fixed charges in the AEL and CEL. The local electric field (shown in green arrows), originates from the protonation and deprotonation of the nanoparticle surface hydroxyls, and further modulated by electronic polarization of free carriers or dielectric inside the nanoparticles, as well as the external electric field. The local electric field induces the water molecules to orient, facilitating WD and proton transfer. M, M′, and M″ denote different sites on the catalyst surface.

(B) Possible electric-potential φ profiles of pristine BPMs and catalyzed BPMs. The hydrogen bond between water molecules is also shown for comparison.

of ~5 (from ~0.002 to ~0.09), when the mass ratio increases from 0% to 150%, but does not change G_0 significantly. Simpler Arrhenius analysis also shows that E_a is lowered (Figure S6), consistent with the BPM-equation analysis. Adding electronically conductive material to the region of WD thus appears to improve kinetics for thick catalyst layers by screening and increasing local-electric-field strength that serves to lower E_a with increasing applied voltage.

A new microscopic model for voltage-driven catalyzed WD

The sum of the kinetic data and analysis led us to propose a new tentative model for WD on metal-oxide surfaces (Figure 5). This new model is relevant not only for BPMs but also for interfacial electrocatalytic processes where WD is required to provide protons, e.g., CO_2 or H_2O reduction in neutral to basic conditions.[17] Acid-base reactions, H^+ and OH^- transfer, and WD all involve the interconversion between O–H and hydrogen bonds. The Grotthuss mechanism of H^+ and OH^- transport in water involves the movement of charge through a series of protonation and deprotonation steps on different water molecules (i.e., the interconversion between O–H bonds and hydrogen bonds and non-vehicular transport). Similar mechanisms could occur on the surface of oxide nanoparticles due to species such as bridging and terminal oxo and hydroxyl groups that can be protonated or deprotonated and that interact strongly with interfacial water that may mediate proton transport.[58,59] The surface of metal oxides thus may serve as a "sink" or "source" of protons that can transport on the nanoparticle surface through the surface oxo/hydroxyl groups. *The oxide surface can thus serve as both proton reservoir and proton conductor.*

Local equilibrium between the WD catalyst and liquid water further leads to interfacial electrostatic effects in the form of a double-layer electric field whenever the local pH is not at the point of zero charge (PZC) of the nanoparticle. The strength of this local interfacial field is likely important for proton transfer reactions between the surface of the catalyst particle and water because the electric field modulates

Please cite this article in press as: Chen et al., Kinetics and mechanism of heterogeneous voltage-driven water-dissociation catalysis, Joule (2023), https://doi.org/10.1016/j.joule.2023.06.011

substantially interface-water structure and properties, like the effective dielectric constant and average orientation.[60–62]

In the BPM junction, however, the situation is further affected by the *external* electric field originating from the uncompensated fixed charges at the AEL and CEL. If the nanoparticle has high electronic conductivity (e.g., IrO_x, $Sb:SnO_2$, etc.), the electrons inside the nanoparticle will redistribute to screen the electric field, and the nanoparticle will be polarized, much like a nanoscale bipolar electrode.[63] These conductive catalysts could even drive faradaic reactions (such as electrolysis) if sufficiently polarized, but for our catalysts, the applied WD overpotential is typically too low for such reactions to occur. WD catalysts with a high dielectric constant (e.g., TiO_2) will similarly screen the electric field inside the particle and increase the electric field outside the particle within the effective Debye length defined by the local ion concentrations and dielectric constant at the particle surface.[64]

In both high-dielectric and conductive particles, the polarization of the particle by the external electric field across the BPM should enhance the local electric field near the nanoparticle surface, driving water molecules to orient and align, on average, their dipole moment with electric field.[62,65] Under reverse-bias operation, i.e., where the BPM is driving WD at the junction, the space-charge regions in the AEL and CEL increase with applied bias, leading to an increasing average electric-field strength across the WD catalyst layer and increasing the degree of water orientation.

We propose that the water organization at the WD catalyst/water interface, driven by the external electric field, is responsible for the experimentally measured pre-exponential factor, i.e., representing a process that describes the fraction of time, and frequency at which, the system is poised for proton transfer. Our model explains the proportionality between A and η_{wd}. As the local electric field increases with η_{wd}, water molecules are, on average, better oriented for donating a proton to one side of the WD catalyst particle (i.e., partial-positive proton on H_2O pointed toward the surface) and accepting a proton on the other side of the WD catalyst (i.e., with the partial-negative O on H_2O pointed toward the surface), as depicted in Figure 5A. The fact that D_2O has a smaller A than H_2O is consistent with the slower vibrational frequency and molecular motions of heavier D_2O.

Although the above argument provides an explanation for how the local electric field, both at equilibrium and increasing with applied reverse bias, might lead to an increase in the pre-exponential factor describing WD kinetics, we must also consider the field effect on the WD activation barrier. In the classic Butler-Volmer model, increasing applied overpotential leads to an increase in electron-transfer rate by lowering activation barrier. The transfer coefficient, typically called α (which can be equated to the symmetry factor β of the free-energy surface for elementary reaction steps),[66] is often taken to be 0.5. This assumption is based on the notion that the electron transfer occurs through the width of the double layer (i.e., it is an outer-sphere process) and that the free-energy surface is symmetric with respect to approach to the transition state. We consider the overall reaction in our analysis and define α here as the proton-transfer coefficient (instead of symmetry factor).

Although we use a similar formulation to describe the rate of proton transfer in WD, the experimental values for the proton-transfer coefficient α are much smaller, i.e.,

Please cite this article in press as: Chen et al., Kinetics and mechanism of heterogeneous voltage-driven water-dissociation catalysis, Joule (2023), https://doi.org/10.1016/j.joule.2023.06.011

from 0 to ~0.04, resulting in a weak E_a dependence on η_{wd} for catalyzed BPMs, compared with typical electrochemical reactions. The electric-field dependence of WD rate has historically been interpreted in the context of the second Wien effect where the strong local field increases the dissociation rate of weak electrolytes, although others have questioned whether a sufficiently strong field in fact exists in the BPM junction.[15,25] Our new experimental data shed light on this fundamental process. Increasing electric field, represented by a larger driving force for WD through η_{wd}, does decrease the experimental activation barrier, supporting the field-effect argument. However, this effect is only significant for BPMs without catalyst that have a narrow junction thickness and hence high electric field (and thus very poor WD and BPM performance).

In BPMs, the electric potential drop mainly occurs at the junction; thus, the *electric potential drop* distance is roughly the junction thickness. For pristine BPMs without catalyst, the junction thickness is ~1–5 nm including the depletion region, interface roughness, and intermixing between AEL and CEL (Figure 5B).[2,67–69] For a hydrogen bond in liquid water (O–H···O), the O–H bond length is ~0.1 nm, and the H···O bond length is ~0.2 nm.[70] Thus, the proton-transfer distance for WD ($2H_2O \rightarrow H_3O^+ + OH^-$) is ~0.1 nm. If we take the junction thickness to be ~2 nm, then, the ratio between proton-transfer distance and the overall potential drop distance is ~0.05, which is comparable with the experimental α of pristine BPMs of ~0.04; that is, only about 5% of the potential drop across the entire interface is available, on average, to facilitate any given proton transfer step.

The situation is more complicated when WD catalysts are introduced because the spatial electric-field profile in the junction, especially near the catalyst surface where WD occurs, is unknown. From previous works, the TiO_2-P25 thickness at optimal loading (0.2 wt%) is ~200 nm.[23] Thus, the ratio between proton-transfer distance and the overall potential drop distance is ~0.0004, which is comparable with the experimental $\alpha \sim 0$ of optimal-loading samples. If the electric field were uniform inside the BPM junction, further increasing the WD catalyst loading and thus junction thickness should decrease α. However, the experimental result for the much thicker 2 wt% is $\alpha \sim 0.002$. By adding ACB, α for similar samples increases to ~0.01. These data suggest that the catalyst screens the electric field inside the nanoparticles, thus focusing the electric field outside the particle where WD takes place. Continuum, molecular dynamics (MDs), and density functional theory (DFT) modeling would help test the above hypothesis.

To test the role of interface-layer thickness, and thus resulting electric-field distribution, in the absence of the catalytic metal-oxide particles, we used polystyrene nanospheres (non-functionalized, diameter of 100 nm). BPMs fabricated with about two layers of the beads on the CEL (to make a ~200 nm spacing between AEL and CEL, similar to the optimal TiO_2 WD catalysts) yield extremely poor performance (Figure S7), much worse than even the pristine BPM. The resulting j-η_{wd} curve, however, was much more linear compared with the pristine BPM, indicating a much smaller α, consistent with the much-lower electric-field strength. We also tested non-catalytic, but electrically conductive, ACB. Although we found BPM junctions with ACB to be unstable at high current, we were able to collect temperature-dependent data at $\leq$50 mA cm^{-2}. Analysis of the data after correction for degradation (like the correction for pristine BPMs, Figure S4) yielded α of 0.02–0.04 (Figure S8), much larger than that for the TiO_2-P25-catalyzed BPM. This finding is consistent with our interpretation of α here and the fact that ACB is an electronic conductor that screens and focuses the electric field to the boundaries of the BPM interfacial layer.

Please cite this article in press as: Chen et al., Kinetics and mechanism of heterogeneous voltage-driven water-dissociation catalysis, Joule (2023), https://doi.org/10.1016/j.joule.2023.06.011

In bulk water, WD occurs through rare electric-field fluctuations, and the generated ions recombine quickly if they are not sufficiently separated.[71] This is likely also the case for the pristine BPM without WD catalyst and why it requires a large η_{wd}. The situation is different when there are nanoparticle catalysts where H_2O can transfer H^+ to the oxide surface that can be transported on the nanoparticle surface toward the CEL, whereas OH^- can be transported in the water "matrix" surrounding the nanoparticles toward the AEL. Thus, one might view the WD catalyst as facilitating the correct configuration of water and surface for successful proton transfer and the WD reaction to occur. Compared with the uncatalyzed BPM, our data show that adding a WD catalyst leads to a dramatic increase in the driving-force-independent proton-transfer conductance G_0, which can be explained by the large number of sites for proton transfer on the catalyst surface. In the isotope experiment, G_0 follows the same dependence on loading for both H_2O and D_2O, and the ratio $G_0(H_2O)/G_0(D_2O)$ is ~10. This is comparable with the ratio of k_D and K_w (Table 1), suggesting that G_0 represents both the number density of catalytic sites and the "intrinsic" WD activity of H_2O and D_2O related to their atomic motions. In the experiment where conducting carbon was added, G_0 does not change because the mass of TiO_2-P25 was kept constant as the mass of carbon was varied. Adding carbon further focuses the electric field, and thus, WD becomes more sensitive to the change in the electric field, which manifests in the increasing α. We further analyzed the relation between E_a and log A to check for compensation effects that have been identified in hydrogen evolution reaction.[37] For catalyzed BPMs, log A is essentially independent of E_a, whereas for pristine BPMs, some correlation is observed (Figure S9).

A molecular interpretation of WD catalysis

We propose a molecular proton-transfer mechanism, where M, M′, and M″ denote different proton acceptor/donor sites on the catalyst surface (Figure 5A):

$$H_2O + MO^- \rightarrow OH^- + MOH \quad \text{(R1)}$$

$$MOH + M'OH \rightarrow MO^- + M'OH_2^+ \quad \text{(R2)}$$

$$M'OH_2^+ + M''OH \rightarrow M'OH + M''OH_2^+ \quad \text{(R3)}$$

$$M''OH_2^+ + H_2O \rightarrow M''OH + H_3O^+ \quad \text{(R4)}$$

This mechanism is reminiscent of the basic and acidic two-step mechanism proposed previously.[15] Here, we use the acidic two-step mechanism (R5 and R6) for discussion, but the basic case is analogous.

$$H_2O + MOH_2^+ \rightarrow MOH + H_3O^+ \; K_5 = K_a \quad \text{(R5)}$$

$$MOH + H_2O \rightarrow MOH_2^+ + OH^- \; K_6 = K_w/K_a. \quad \text{(R6)}$$

In the previously proposed two-step mechanisms,[15] there is an underlying assumption that the catalytic cycle occurs on the same site, which means that H_3O^+ and OH^- are produced in close proximity. This constrains the optimal K_a of the example MOH_2^+ site; if the K_a is large (more acidic), then, R5 is more favored (and usually faster), but this means that R6 is less favored (and usually slower) because its equilibrium constant is K_w/K_a (if we assume a constant K_w). This is why previous calculations conclude that a pK_a (or equivalently pK_b) of ~7 of the catalytic site should give the best performance.[30]

Please cite this article in press as: Chen et al., Kinetics and mechanism of heterogeneous voltage-driven water-dissociation catalysis, Joule (2023), https://doi.org/10.1016/j.joule.2023.06.011

The new mechanism proposed here involving surface proton transfer (R2 and R3) enables R1 and R4 to occur at different sites (M and M″) on the catalyst surface and thus generate H_3O^+ and OH^- that are separated in space. The K_a of the M and M″ site are less constrained than those in the single-site model. The M site could be basic so that R1 is favored and fast, whereas M″ site could be acidic so that R4 is favored and fast, and the relevant surface K_a will also depend on the degree of polarization of the nanoparticle catalysts.[72] The rate-determining step likely depends on the WD catalyst type because chemically different surfaces will have different acid-base behavior and surface proton-adsorption isotherms. When the loading is small, R1 or R4 might be rate determining. Since these two steps might be more sensitive to the local electric field, we might observe a larger α. In contrast, at optimal loading, the surface-transport steps (R2 and R3) might be rate determining leading to ohmic behavior ($\alpha = 0$), as the experiment shows. Interestingly, we note that theoretical calculations find a free-energy barrier of 25 $\pm$ 4 kJ mol^{-1} for proton transfer and 32 $\pm$ 4 kJ mol^{-1} for dissociative adsorption of water on the TiO_2 anatase (101) surface in water,[59] values similar to our experimental results. R2 and R3 thus may have a free energy barrier of ~25 kJ mol^{-1}, whereas for R1 and R4, it may be ~32 kJ mol^{-1}.

Conclusions

We developed a membrane-potential-sensing method with two integrated REs in BPM electrolyzers to directly measure the WD overpotential. Through variable-temperature studies and Arrhenius-type analysis with TiO_2-P25 as a model, but effective, WD catalyst, we found that the apparent activation energy E_a only weakly depends on η_{wd}, whereas the pre-exponential factor A is directly proportional to η_{wd}. D_2O requires higher η_{wd} to drive WD than H_2O, but surprisingly, the E_a are similar, and the higher η_{wd} is due to the lower pre-exponential factor. Electronically conducting ACB improves the performance by lowering E_a, consistent with a field-focusing effect. We developed a BPM equation with three parameters to quantitatively describe the temperature-dependent kinetics and discussed the physical meaning of these parameters. We proposed a new molecular mechanism involving rate-determining proton transfer to/from water and proton transport across the catalyst surface under applied voltage. These findings provide insights into—and inspire new strategies for the development of—other electrochemical process where WD is relevant, e.g., alkaline HER and CO_2 electroreduction.[21,45,46]

One limitation of the present work is the lack of direct evidence for the proposed mechanism due to the inherent difficulty of studying buried interfaces like the BPM junction. More experimental and computational studies, at an appropriately high level of theory that captures the molecular details of water and surfaces, are needed to test the new model presented here. The proposed BPM equation is also semi-empirical. Developing an analytical formalism based on a detailed molecular mechanism remains challenging due to the complexity of the BPM junction and it being a buried interface. A general equation for the current density in a one-dimensional model is

$$j = F \int_{BPM} \left(k_D c_{H_2O} - k_R c_{H^+} c_{OH^-} \right) dx \qquad \text{(Equation 9)}$$

where k_D and k_R are net dissociation and recombination reaction rate constants, c is the concentration, and x is the coordinate perpendicular to the planar junction. The values for k_D, k_R, and c probably all depend on x, η_{wd} or electric field, and the details of the catalyst.[73,74] However, there is no experimental data regarding the electric potential/field and H_2O, H^+, and OH^- concentration profiles in the BPM junction. *Operando*

Please cite this article in press as: Chen et al., Kinetics and mechanism of heterogeneous voltage-driven water-dissociation catalysis, Joule (2023), https://doi.org/10.1016/j.joule.2023.06.011

measurements of pH, pOH, and electric-field profiles in the BPM junction, perhaps with fluorescent indicators and Stark-effect-based probes, would be valuable.[75]

Accurate simulations of the interface molecular and continuum chemistry and physics of the system are also needed.[68,76] MD and DFT calculations to test the various proton-transfer WD-reaction mechanisms at nanoparticle/water interface under a strong electric field will provide insights into elementary reaction barriers and reaction pathways. We also note that in the Eyring equation from transition-state theory, the pre-exponential factor A is related to the entropy of activation $\Delta S^{\ddagger}$.[77] Our observation that A is proportional to η_{wd} may also mean that $\Delta S^{\ddagger}$ changes with η_{wd}, which can be elucidated by theory and computation. It also remains unclear whether all the nanoparticles participate in the WD reaction or only those near the AEL and CEL. At the molecular scale, we do not know what sites are active for WD on the surface. We presume the bridging and/or terminal oxo/hydroxyl species are the active sites as proton acceptors or donors, but there may be other WD sites. Molecularly precise analogs would be of value to study, for example, small molecules with well-defined pK_a's can be tethered to surfaces of nanoparticles (e.g., –COOH, $–NH_2$, $–PO_3H$ from commercial silanes, etc.).

Nonetheless, the developed BPM equation sets a foundation for WD catalyst development and future fundamental studies. Any theory should reduce to the semi-empirical equation under appropriate assumptions. The BPM equation also does not explicitly separate the forward WD reaction and reverse H^+/OH^- recombination reaction, which may proceed via different mechanisms or with different rate-determining steps. With further experimental optimization, future work could assess larger ranges of current and η_{wd} to better determine the α values that describe the reaction kinetics. Temperature-dependence and kinetic-isotopic-effect experiments for different WD catalysts in both forward and reverse bias (to obtain full polarization curves) are needed, probably using a H_2-pump-type cell instead of a water electrolyzer platform.[78]

EXPERIMENTAL PROCEDURES

Resource availability

Lead contact

Further information and request for resources and materials should be directed to and will be fulfilled by the lead contact, Shannon Boettcher (swb@uoregon.edu).

Materials availability

This study did not generate new unique reagents. Bipolar membranes created in this study are available by reasonable request from the lead author.

Data and code availability

The data presented in this work are deposited in the Science Data Bank (https://doi.org/10.57760/sciencedb.08522).

Bipolar membrane fabrication and measurements

The experimental procedures are modified from our previous report.[23] The anode gas-diffusion electrode/layer (GDE/GDL) was fabricated by spray coating one vial of anode ink (dispersed by sonication), containing 0.2 g Co_3O_4 (30–50 nm, US Research Nanomaterials), 1.0 g H_2O, 3.4 g isopropyl alcohol (IPA), and 0.2 g PiperION-A5 Ionomer Suspension (TP-85, 5% w/w, Versogen), onto a 5 cm × 5 cm stainless steel 25AL3 (Bekaert Bekipor) support taped on a hot plate of 90°C. The loading was ~2 mg cm^{-2}. Then PiperION-A5 ionomer suspension (as received) was sprayed onto the catalysts until the mass of the ionomer reached 10%–20% of

Please cite this article in press as: Chen et al., Kinetics and mechanism of heterogeneous voltage-driven water-dissociation catalysis, Joule (2023), https://doi.org/10.1016/j.joule.2023.06.011

the catalyst mass. The GDL was cut into 1.0 cm × 1.0 cm coupons. The cathode GDL was fabricated in a similar way with Toray Carbon Paper 090 (wet proofed, Fuel Cell Store) as the substrate, and two vials of ink containing 0.1 g Pt black (high surface area, Fuel Cell Store), 1.5 g H_2O, 1.7 g IPA, 0.1 g D520 Nafion dispersion (alcohol-based 1000 EW at 5 wt%, Fuel Cell Store).

PiperION-A40-HCO3 (TP-85, 40-μm thick, Versogen) membrane was soaked in 0.5 M KOH for >1 h, stored in fresh 0.5 M KOH, and rinsed in ultrapure H_2O before being used as the AEL. The Nafion 212 (Fuel Cell Store) membrane was soaked and stored in H_2O and used as the CEL. Both membranes are cut into 1.5 cm × 1.5 cm for use as the AEL and CEL in the BPM, and 1.5 cm × 7.5 cm as the AEL and CEL sensing strips. The WD catalyst was spin-coated onto the CEL. TiO_2-P25 (Aeroxide Nippon Aerosil) was dispersed in a H_2O/IPA mixture (1:1 by weight) with different wt% solids to make the ink. The edges of a CEL (1.5 cm × 1.5 cm) were taped on a glass slide. The ink was added onto CEL until fully covered and then the sample spun at 3,000 rpm for 30 s to create a uniform thin layer of WD catalyst. Polystyrene beads (Alpha Nanotech, non-functionalized, 100 nm, 10 mg/mL) were diluted with IPA to make a 0.5 wt% dispersion in H_2O/IPA mixture (1:1 by weight) and spun twice onto the CEL in the same way.

Due to the poor dispersibility of ACB, spin coating does not give good quality catalyst coating. Therefore, spray coating was used. A 2 wt% mother ink of TiO_2-P25 was prepared in water and sonicated until well dispersed. Based on the target mass ratio of ACB and TiO_2-P25, ACB was weighed in a 20 mL vial (e.g., 50 wt% required 2 mg of ACB), then 200 mg of the 2 wt% TiO_2-P25 mother ink (equivalent to 4 mg of TiO_2-P25) is added. Water is added until the total mass reaches 0.5 g, then 1.7 g of IPA is added and the mixture is sonicated until well dispersed. A CEL of 1.5 cm × 1.5 cm is taped on a Petri dish and placed on a hot plate of 90°C. The ink is spray coated onto the CEL. To improve the uniformity, the dish is rotated 90° every 10 spray bursts. After spraying, the tapes were removed and the coated CEL was moved into pure water for later use.

The electrolyzer uses PEM fuel-cell hardware (Fuel Cell Store) with the original graphite anode flow field replaced by a homemade stainless steel one. For step-by-step procedures regarding cell construction and assembly, see the supplemental experimental procedures. The active geometric area (1 cm^2) is defined by the gaskets and current is normalized to this geometric area to give current density in all the provided plots. Ultrapure H_2O (18.2 MΩ cm) heated at different temperatures was fed to both the anode and cathode so that the electrolyzer temperature was 25°C, 35°C, 45°C, or 55°C ± 2°C (error estimated as the maximum fluctuation). D_2O (99.9%, Cambridge Isotope Laboratories) is used instead of H_2O for kinetic-isotope effect experiments. Conventionally, Ag|AgCl REs are usually used measure WD voltage of BPMs in H-cells, but the frits dissolve in strong base and the potentials are unreliable due to formation of AgO. We used a saturated calomel electrode (SCE) in 0.1 M H_2SO_4 and a Hg|HgO RE in 0.1 M KOH. The WD voltage V_{wd} was then measured as $V_{wd} = V_{wd}^{raw} + \Delta V_{RE}$, where V_{wd}^{raw} is the as-measured voltage between Hg|HgO and SCE during test, and ΔV_{RE} = 0.136 V (measured in saturated KCl solution) is the correction factor for the difference between Hg|HgO and SCE in the same solution at equilibrium without the effect of transmembrane voltages. To calculate η_{wd}, it is not strictly necessary to correct for ΔV_{RE} as

$$\eta_{wd} \equiv V_{wd} - V_{wd,eq} = \left(V_{wd}^{raw} + \Delta V_{RE}\right) - \left(V_{wd,eq}^{raw} + \Delta V_{RE}\right) = V_{wd}^{raw} - V_{wd,eq}^{raw} \quad \text{(Equation 10)}$$

where the subscript "eq" denotes the equilibrium value, i.e., when current density j = 0 mA cm^{-2}.

The ionic conductivity of the AEL (PiperION TP-85) at 25°C is ~80 mS cm^{-1}. With a thickness of 40 μm, the areal ionic resistance of the AEL is ~0.05 Ω cm^2.[79] The reported ionic conductivity of the CEL (Nafion 212) ranges from ~50 to ~100 mS cm^{-1} at 30°C.[80,81] Assuming it is ~75 mS cm^{-1} and a thickness of 50 μm, the areal ionic resistance of the CEL is ~0.07 Ω cm^2. The measured R_{wd} is ~0.6 Ω cm^2 for optimal TiO_2-P25 loading at 25°C (Figure S1) and only about half of the combined AEL and CEL ohmic voltage drop is measured along with η_{wd} using our membrane potential sensing approach. We thus ignore effects of AEL and CEL ionic resistance in our analyses.

The electrochemical tests were performed with a two-channel BioLogic VSP-300 potentiostat. For channel 1, the P1 and S1 leads were connected to the anode current collector; P2, S2, and S3 were connected to the cathode current collector (P, power lead; S, sense lead). For channel 2, S1 was connected to the Hg|HgO RE, S2 to the cathode current collector, and S3 to the SCE RE. P1 and P2 were not used. Channel 1 and channel 2 are synchronized during the experiment. Channel 2 records voltage every 0.1 s. The current was applied by channel 1 and stepped up at j = 10, 50, 100, 150, …, 500 mA cm^{-2} (10 s each step) and held at 500 mA cm^{-2} for 10 min (if the voltage exceeds the maximum range of the potentiostat, then held at the highest j). Then galvanostatic EIS (GEIS) was measured from 600 kHz to 60 mHz with four points per decade at 500, 450, 400, …, 100, 50, 40, 30, 20, 10, and 5 mA cm^{-2} with an alternating current (AC) amplitude of 6% of the applied direct current (DC) density (for 10 and 5 mA cm^{-2}, an amplitude of 1 mA cm^{-2} was used). The impedance data were fit with impedance.py.[82,83] The $R(j)$ plot is extrapolated by cubic spline to j = 0 mA cm^{-2} so that the integral $\eta_{wd} = \int_0^j R_{wd}(j)dj$ begins at 0. For the temperature-dependent tests, after GEIS, j was stepped up again (5 s each step) and held at 500 mA cm^{-2} for 2 min. Then, j was stepped down at 500, 450, 400, …, 100, 50, 40, 30, 20, 10, and 5 mA cm^{-2} (5 s each step). The last three seconds of each step was averaged to produce the polarization curves. For the BPM without catalyst, j was decreased by a factor of 100 to prevent large voltage polarizations. The temperature was then changed, and the procedure was repeated. Temperatures from 25°C to 55°C (every 10°C) and back to 25°C were used. Two temperature cycles were performed for each test. A degradation (increase in voltage) was sometimes observed in the first temperature step-up process for low-catalyst-loading samples, after which the performance (at the same temperature) was repeatable during cycling. Thus, the first 25°C, 35°C, and 45°C data were not used for the temperature-dependence analysis for those samples (Figure S2).

SUPPLEMENTAL INFORMATION

Supplemental information can be found online at https://doi.org/10.1016/j.joule.2023.06.011.

ACKNOWLEDGMENTS

This work was supported by the U.S. Office of Naval Research, grant N00014-20-1-2517 (S.W.B). Q.X. acknowledges the China Scholarship Council and Excellent PhD Development Program from ECUST. Sebastian Oener is acknowledged for assistance developing the membrane-potential-sensing technique, and Shane Ardo and Sayantan Sasmal for useful discussions of WD mechanisms and kinetics. The work made use of shared instrumentation in the Center for Advanced Materials

Characterization in Oregon (CAMCOR) and the Phil and Penny Knight Campus for Accelerating Scientific Impact.

AUTHOR CONTRIBUTIONS

S.W.B. conceived the experiments and led the project. L.C. performed most experiments. Q.X. and L.C. performed pilot experiments. L.C. and S.W.B. wrote the manuscript with input from all authors.

DECLARATION OF INTERESTS

The authors have filed a provisional patent on aspects of the work.

Received: January 31, 2023
Revised: May 7, 2023
Accepted: June 12, 2023
Published: July 10, 2023

REFERENCES

1. Giesbrecht, P.K., and Freund, M.S. (2020). Recent advances in bipolar membrane design and applications. Chem. Mater. *32*, 8060–8090. https://doi.org/10.1021/acs.chemmater.0c02829.

2. Pärnamäe, R., Mareev, S., Nikonenko, V., Melnikov, S., Sheldeshov, N., Zabolotskii, V., Hamelers, H.V.M., and Tedesco, M. (2021). Bipolar membranes: a review on principles, latest developments, and applications. J. Membr. Sci. *617*, 118538. https://doi.org/10.1016/j.memsci.2020.118538.

3. Blommaert, M.A., Aili, D., Tufa, R.A., Li, Q., Smith, W.A., and Vermaas, D.A. (2021). Insights and challenges for applying bipolar membranes in advanced electrochemical energy systems. ACS Energy Lett. *6*, 2539–2548. https://doi.org/10.1021/acsenergylett.1c00618.

4. Yan, Z., and Mallouk, T.E. (2021). Bipolar membranes for ion management in (photo) electrochemical energy conversion. Acc. Mater. Res. *2*, 1156–1166. https://doi.org/10.1021/accountsmr.1c00113.

5. Miesiac, I., and Rukowicz, B. (2022). Bipolar membrane and water splitting in electrodialysis. Electrocatalysis *13*, 101–107. https://doi.org/10.1007/s12678-021-00703-5.

6. Strathmann, H. (2010). Electrodialysis, a mature technology with a multitude of new applications. Desalination *264*, 268–288. https://doi.org/10.1016/j.desal.2010.04.069.

7. Shehzad, M.A., Yasmin, A., Ge, X., Ge, Z., Zhang, K., Liang, X., Zhang, J., Li, G., Xiao, X., Jiang, B., et al. (2021). Shielded goethite catalyst that enables fast water dissociation in bipolar membranes. Nat. Commun. *12*, 9. https://doi.org/10.1038/s41467-020-20131-1.

8. Fu, R., Wang, H., Yan, J., Li, R., Jiang, C., Wang, Y., and Xu, T. (2023). Asymmetric bipolar membrane electrodialysis for acid and base production. AIChE J. *69*, e17957. https://doi.org/10.1002/aic.17957.

9. Lu, H., Wang, L., Wycisk, R., Pintauro, P.N., and Lin, S. (2020). Quantifying the kinetics-energetics performance tradeoff in bipolar membrane electrodialysis. J. Membr. Sci. *612*, 118279. https://doi.org/10.1016/j.memsci.2020.118279.

10. Bazinet, L., Lamarche, F., and Ippersiel, D. (1998). Bipolar-membrane electrodialysis: applications of electrodialysis in the food industry. Trends Food Sci. Technol. *9*, 107–113. https://doi.org/10.1016/S0924-2244(98)00026-0.

11. Tongwen, X. (2002). Electrodialysis processes with bipolar membranes (EDBM) in environmental protection—a review. Resour. Conserv. Recycl. *37*, 1–22. https://doi.org/10.1016/S0921-3449(02)00032-0.

12. Ahlfield, J.M., Liu, L., and Kohl, P.A. (2017). PEM/AEM junction design for bipolar membrane fuel cells. J. Electrochem. Soc. *164*. F1165–F1171. https://doi.org/10.1149/2.1041712jes.

13. Peng, S., Xu, X., Lu, S., Sui, P.-C., Djilali, N., and Xiang, Y. (2015). A self-humidifying acidic–alkaline bipolar membrane fuel cell. J. Power Sources *299*, 273–279. https://doi.org/10.1016/j.jpowsour.2015.08.104.

14. Yan, Z., Wycisk, R.J., Metlay, A.S., Xiao, L., Yoon, Y., Pintauro, P.N., and Mallouk, T.E. (2021). High-voltage aqueous redox flow batteries enabled by catalyzed water dissociation and acid–base neutralization in bipolar membranes. ACS Cent. Sci. *7*, 1028–1035. https://doi.org/10.1021/acscentsci.1c00217.

15. Oener, S.Z., Foster, M.J., and Boettcher, S.W. (2020). Accelerating water dissociation in bipolar membranes and for electrocatalysis. Science *369*, 1099–1103. https://doi.org/10.1126/science.aaz1487.

16. Powers, D., Mondal, A.N., Yang, Z., Wycisk, R., Kreidler, E., and Pintauro, P.N. (2022). Freestanding bipolar membranes with an electrospun junction for high current density water splitting. ACS Appl. Mater. Interfaces *14*, 36092–36104. https://doi.org/10.1021/acsami.2c07680.

17. Xie, K., Miao, R.K., Ozden, A., Liu, S., Chen, Z., Dinh, C.-T., Huang, J.E., Xu, Q., Gabardo, C.M., Lee, G., et al. (2022). Bipolar membrane electrolyzers enable high single-pass CO_2 electroreduction to multicarbon products. Nat. Commun. *13*, 3609. https://doi.org/10.1038/s41467-022-31295-3.

18. Blommaert, M.A., Sharifian, R., Shah, N.U., Nesbitt, N.T., Smith, W.A., and Vermaas, D.A. (2021). Orientation of a bipolar membrane determines the dominant ion and carbonic species transport in membrane electrode assemblies for CO_2 reduction. J. Mater. Chem. A Mater. *9*, 11179–11186. https://doi.org/10.1039/D0TA12398F.

19. Marin, D.H., Perryman, J.T., Hubert, M.A., Lindquist, G.A., Chen, L., Aleman, A.M., Kamat, G.A., Niemann, V.A., Stevens, M.B., Regmi, Y.N., et al. (2023). Hydrogen production with seawater-resilient bipolar membrane electrolyzers. Joule *7*, 765–781. https://doi.org/10.1016/j.joule.2023.03.005.

20. Subbaraman, R., Tripkovic, D., Strmcnik, D., Chang, K.C., Uchimura, M., Paulikas, A.P., Stamenkovic, V., and Markovic, N.M. (2011). Enhancing hydrogen evolution activity in water splitting by tailoring Li^+-$Ni(OH)_2$-Pt interfaces. Science *334*, 1256–1260. https://doi.org/10.1126/science.1211934.

21. McCrum, I.T., and Koper, M.T.M. (2020). The role of adsorbed hydroxide in hydrogen evolution reaction kinetics on modified platinum. Nat. Energy *5*, 891–899. https://doi.org/10.1038/s41560-020-00710-8.

22. Marcandalli, G., Monteiro, M.C.O., Goyal, A., and Koper, M.T.M. (2022). Electrolyte effects on CO_2 electrochemical reduction to CO. Acc. Chem. Res. *55*, 1900–1911. https://doi.org/10.1021/acs.accounts.2c00080.

23. Chen, L., Xu, Q., Oener, S.Z., Fabrizio, K., and Boettcher, S.W. (2022). Design principles for water dissociation catalysts in high-performance bipolar membranes. Nat. Commun. *13*, 3846. https://doi.org/10.1038/s41467-022-31429-7.

24. Onsager, L. (1934). Deviations from Ohm's law in weak electrolytes. J. Chem. Phys. *2*, 599–615. https://doi.org/10.1063/1.1749541.

Please cite this article in press as: Chen et al., Kinetics and mechanism of heterogeneous voltage-driven water-dissociation catalysis, Joule (2023), https://doi.org/10.1016/j.joule.2023.06.011

25. Kunst, B., and Lovreček, B. (1962). Electrochemical properties of the ion-exchange membranes junction. II. Croat. Chem. Acta *34*, 219–229.

26. Cai, J., Griffin, E., Guarochico-Moreira, V.H., Barry, D., Xin, B., Yagmurcukardes, M., Zhang, S., Geim, A.K., Peeters, F.M., and Lozada-Hidalgo, M. (2022). Wien effect in interfacial water dissociation through proton-permeable graphene electrodes. Nat. Commun. *13*, 5776. https://doi.org/10.1038/s41467-022-33451-1.

27. Cai, J., Griffin, E., Guarochico-Moreira, V., Barry, D., Xin, B., Huang, S., Geim, A.K., Peeters, F.M., and Lozada-Hidalgo, M. (2022). Photoaccelerated water dissociation across one-atom-thick electrodes. Nano Lett. *22*, 9566–9570. https://doi.org/10.1021/acs.nanolett.2c03701.

28. Simons, R., and Khanarian, G. (1978). Water dissociation in bipolar membranes: experiments and theory. J. Membrain. Biol. *38*, 11–30. https://doi.org/10.1007/BF01875160.

29. Simons, R. (1979). Strong electric field effects on proton transfer between membrane-bound amines and water. Nature *280*, 824–826. https://doi.org/10.1038/280824a0.

30. Strathmann, H., Krol, J.J., Rapp, H.J., and Eigenberger, G. (1997). Limiting current density and water dissociation in bipolar membranes. J. Membr. Sci. *125*, 123–142. https://doi.org/10.1016/S0376-7388(96)00185-8.

31. Yan, Z., Zhu, L., Li, Y.C., Wycisk, R.J., Pintauro, P.N., Hickner, M.A., and Mallouk, T.E. (2018). The balance of electric field and interfacial catalysis in promoting water dissociation in bipolar membranes. Energy Environ. Sci. *11*, 2235–2245. https://doi.org/10.1039/C8EE01192C.

32. Ramírez, P., Rapp, H.J., Reichle, S., Strathmann, H., and Mafé, S. (1992). Current-voltage curves of bipolar membranes. J. Appl. Phys. *72*, 259–264. https://doi.org/10.1063/1.352124.

33. Aritomi, T., van den Boomgaard, T., and Strathmann, H. (1996). Current-voltage curve of a bipolar membrane at high current density. Desalination *104*, 13–18. https://doi.org/10.1016/0011-9164(96)00021-5.

34. Hurwitz, H.D., and Dibiani, R. (2001). Investigation of electrical properties of bipolar membranes at steady state and with transient methods. Electrochim. Acta *47*, 759–773. https://doi.org/10.1016/S0013-4686(01)00757-5.

35. Hurwitz, H.D., and Dibiani, R. (2004). Experimental and theoretical investigations of steady and transient states in systems of ion exchange bipolar membranes. J. Membr. Sci. *228*, 17–43. https://doi.org/10.1016/j.memsci.2003.09.009.

36. He, Z.-D., Chen, Y.-X., Santos, E., and Schmickler, W. (2018). The pre-exponential factor in electrochemistry. Angew. Chem. Int. Ed. Engl. *57*, 7948–7956. https://doi.org/10.1002/anie.201800130.

37. Narangoda, P., Spanos, I., Masa, J., Schlögl, R., and Zeradjanin, A.R. (2022). Electrocatalysis beyond 2020: how to tune the preexponential frequency factor. ChemElectroChem *9*, e202101278. https://doi.org/10.1002/celc.202101278.

38. Zeradjanin, A.R., Narangoda, P., Masa, J., and Schlögl, R. (2022). What controls activity trends of electrocatalytic hydrogen evolution reaction? Activation energy versus frequency factor. ACS Catal. *12*, 11597–11605. https://doi.org/10.1021/acscatal.2c02964.

39. Zeradjanin, A.R., Grote, J.-P., Polymeros, G., and Mayrhofer, K.J.J. (2016). A critical review on hydrogen evolution electrocatalysis: re-exploring the volcano-relationship. Electroanalysis *28*, 2256–2269. https://doi.org/10.1002/elan.201600270.

40. Oener, S.Z., Twight, L.P., Lindquist, G.A., and Boettcher, S.W. (2021). Thin cation-exchange layers enable high-current-density bipolar membrane electrolyzers via improved water transport. ACS Energy Lett. *6*, 1–8. https://doi.org/10.1021/acsenergylett.0c02078.

41. Xu, Q., Oener, S.Z., Lindquist, G., Jiang, H., Li, C., and Boettcher, S.W. (2021). Integrated reference electrodes in anion-exchange-membrane electrolyzers: impact of stainless-steel gas-diffusion layers and internal mechanical pressure. ACS Energy Lett. *6*, 305–312. https://doi.org/10.1021/acsenergylett.0c02338.

42. Adler, S.B. (2002). Reference electrode placement in thin solid electrolytes. J. Electrochem. Soc. *149*, E166. https://doi.org/10.1149/1.1467368.

43. He, W., and Nguyen, T.V. (2004). Edge effects on reference electrode measurements in PEM fuel cells. J. Electrochem. Soc. *151*, A185. https://doi.org/10.1149/1.1634272.

44. Zeng, R., Slade, R.C.T., and Varcoe, J.R. (2010). An experimental study on the placement of reference electrodes in alkaline polymer electrolyte membrane fuel cells. Electrochim. Acta *56*, 607–619. https://doi.org/10.1016/j.electacta.2010.08.032.

45. Intikhab, S., Snyder, J.D., and Tang, M.H. (2017). Adsorbed hydroxide does not participate in the volmer step of alkaline hydrogen electrocatalysis. ACS Catal. *7*, 8314–8319. https://doi.org/10.1021/acscatal.7b02787.

46. Huang, B., Rao, R.R., You, S., Hpone Myint, K., Song, Y., Wang, Y., Ding, W., Giordano, L., Zhang, Y., Wang, T., et al. (2021). Cation- and pH-dependent hydrogen evolution and oxidation reaction kinetics. JACS Au *1*, 1674–1687. https://doi.org/10.1021/jacsau.1c00281.

47. Eigen, M., De Maeyer, L., and Bernal, J.D. (1958). Self-dissociation and protonic charge transport in water and ice. Proc. R. Soc. Lond. A *247*, 505–533. https://doi.org/10.1098/rspa.1958.0208.

48. Ertl, G., and Gerischer, H. (1962). Ein vergleich der kinetik der neutralisationsreaktionen des leichten und schweren wassers. Z. Elecktrochem *66*, 560. https://doi.org/10.1002/bbpc.19620660708.

49. Natzle, W.C., and Moore, C.B. (1985). Recombination of hydrogen ion (H^+) and hydroxide in pure liquid water. J. Phys. Chem. *89*, 2605–2612. https://doi.org/10.1021/j100258a035.

50. Shoesmith, D.W., and Lee, W. (1976). The ionization constant of heavy water (D_2O) in the temperature range 298 to 523 K. Can. J. Chem. *54*, 3553–3558. https://doi.org/10.1139/v76-511.

51. Eigen, M., and Maeyer, L.D. (1955). Untersuchungen über die Kinetik der neutralisation. I. Z. Elektrochem. *59*, 986. https://doi.org/10.1002/bbpc.19550591020.

52. Sweeton, F.H., Mesmer, R.E., and Baes, C.F. (1974). Acidity measurements at elevated temperatures. VII. Dissociation of water. J. Solut. Chem. *3*, 191–214. https://doi.org/10.1007/BF00645633.

53. Yang, Y., Agarwal, R.G., Hutchison, P., Rizo, R., Soudackov, A.V., Lu, X., Herrero, E., Feliu, J.M., Hammes-Schiffer, S., Mayer, J.M., and Abruña, H.D. (2023). Inverse kinetic isotope effects in the oxygen reduction reaction at platinum single crystals. Nat. Chem. *15*, 271–277. https://doi.org/10.1038/s41557-022-01084-y.

54. Mills, R. (1973). Self-diffusion in normal and heavy water in the range 1–45°. J. Phys. Chem. *77*, 685–688. https://doi.org/10.1021/j100624a025.

55. Haynes, W.M., Lide, D.R., and Bruno, T.J. (2017). CRC Handbook of Chemistry and Physics: A Ready-Reference Book of Chemical and Physical Data, Ninety-Seventh Edition (CRC Press).

56. Lee, S.H., and Rasaiah, J.C. (2011). Proton transfer and the mobilities of the H^+ and OH^- ions from studies of a dissociating model for water. J. Chem. Phys. *135*, 124505. https://doi.org/10.1063/1.3632990.

57. Gierer, A. (1950). Anomale D^+ -und OD^- -ionenbeweglichkeit in schwerem wasser. Z. Naturforsch. A *5*, 581–589. https://doi.org/10.1515/zna-1950-1102.

58. Bourikas, K., Kordulis, C., and Lycourghiotis, A. (2014). Titanium dioxide (anatase and rutile): surface chemistry, liquid–solid interface chemistry, and scientific synthesis of supported catalysts. Chem. Rev. *114*, 9754–9823. https://doi.org/10.1021/cr300230q.

59. Calegari Andrade, M.F., Ko, H.-Y., Zhang, L., Car, R., and Selloni, A. (2020). Free energy of proton transfer at the water–TiO_2 interface from *ab initio* deep potential molecular dynamics. Chem. Sci. *11*, 2335–2341. https://doi.org/10.1039/C9SC05116C.

60. Bockris, J.O.M., Devanathan, M.A.V., and Müller, K. (1963). On the structure of charged interfaces. Proc. R. Soc. A Math. Phys. Eng. Sci. *274*, 55–79. https://doi.org/10.1098/rspa.1963.0114.

61. Willard, A.P., Reed, S.K., Madden, P.A., and Chandler, D. (2009). Water at an electrochemical interface—a simulation study. Faraday Discuss. *141*, 423–441. https://doi.org/10.1039/B805544K.

62. Gonella, G., Backus, E.H.G., Nagata, Y., Bonthuis, D.J., Loche, P., Schlaich, A., Netz, R.R., Kühnle, A., McCrum, I.T., Koper, M.T.M., et al. (2021). Water at charged interfaces. Nat. Rev. Chem. *5*, 466–485. https://doi.org/10.1038/s41570-021-00293-2.

63. Fosdick, S.E., Knust, K.N., Scida, K., and Crooks, R.M. (2013). Bipolar electrochemistry. Angew. Chem. Int. Ed. Engl. *52*, 10438–10456. https://doi.org/10.1002/anie.201300947.

Please cite this article in press as: Chen et al., Kinetics and mechanism of heterogeneous voltage-driven water-dissociation catalysis, Joule (2023), https://doi.org/10.1016/j.joule.2023.06.011

64. Guerrero García, G.I., and Olvera de la Cruz, M. (2014). Polarization effects of dielectric nanoparticles in aqueous charge-asymmetric electrolytes. J. Phys. Chem. B *118*, 8854–8862. https://doi.org/10.1021/jp5045173.

65. Mafé, S., Ramírez, P., and Alcaraz, A. (1998). Electric field-assisted proton transfer and water dissociation at the junction of a fixed-charge bipolar membrane. Chem. Phys. Lett. *294*, 406–412. https://doi.org/10.1016/S0009-2614(98)00877-X.

66. Bockris, J.O.M., and Nagy, Z. (1973). Symmetry factor and transfer coefficient: a source of confusion in electrode kinetics. J. Chem. Educ. *50*, 839. https://doi.org/10.1021/ed050p839.

67. Wrubel, J.A., Chen, Y., Ma, Z., and Deutsch, T.G. (2020). Modeling water electrolysis in bipolar membranes. J. Electrochem. Soc. *167*, 114502. https://doi.org/10.1149/1945-7111/ab9ccb.

68. Bui, J.C., Digdaya, I., Xiang, C., Bell, A.T., and Weber, A.Z. (2020). Understanding multi-ion transport mechanisms in bipolar membranes. ACS Appl. Mater. Interfaces *12*, 52509–52526. https://doi.org/10.1021/acsami.0c12686.

69. Mareev, S.A., Evdochenko, E., Wessling, M., Kozaderova, O.A., Niftaliev, S.I., Pismenskaya, N.D., and Nikonenko, V.V. (2020). A comprehensive mathematical model of water splitting in bipolar membranes: impact of the spatial distribution of fixed charges and catalyst at bipolar junction. J. Membr. Sci. *603*, 118010. https://doi.org/10.1016/j.memsci.2020.118010.

70. Chen, B., Ivanov, I., Klein, M.L., and Parrinello, M. (2003). Hydrogen bonding in water. Phys. Rev. Lett. *91*, 215503. https://doi.org/10.1103/PhysRevLett.91.215503.

71. Geissler, P.L., Dellago, C., Chandler, D., Hutter, J., and Parrinello, M. (2001). Autoionization in liquid water. Science *291*, 2121–2124. https://doi.org/10.1126/science.1056991.

72. Delley, M.F., Nichols, E.M., and Mayer, J.M. (2021). Interfacial acid–base equilibria and electric fields concurrently probed by *in situ* surface-enhanced infrared spectroscopy. J. Am. Chem. Soc. *143*, 10778–10792. https://doi.org/10.1021/jacs.1c05419.

73. Stuve, E.M. (2012). Ionization of water in interfacial electric fields: an electrochemical view. Chem. Phys. Lett. *519–520*, 1–17. https://doi.org/10.1016/j.cplett.2011.09.040.

74. Che, F., Gray, J.T., Ha, S., Kruse, N., Scott, S.L., and McEwen, J.-S. (2018). Elucidating the roles of electric fields in catalysis: a perspective. ACS Catal. *8*, 5153–5174. https://doi.org/10.1021/acscatal.7b02899.

75. Yan, Z., Hitt, J.L., Zeng, Z., Hickner, M.A., and Mallouk, T.E. (2021). Improving the efficiency of CO_2 electrolysis by using a bipolar membrane with a weak-acid cation exchange layer. Nat. Chem. *13*, 33–40. https://doi.org/10.1038/s41557-020-00602-0.

76. Bui, J.C., Corpus, K.R.M., Bell, A.T., and Weber, A.Z. (2021). On the nature of field-enhanced water dissociation in bipolar membranes. J. Phys. Chem. C *125*, 24974–24987. https://doi.org/10.1021/acs.jpcc.1c08276.

77. Doyle, P.J., Savara, A., and Raiman, S.S. (2020). Extracting meaningful standard enthalpies and entropies of activation for surface reactions from kinetic rates. React. Kinet. Mech. Catal. *129*, 551–581. https://doi.org/10.1007/s11144-020-01747-2.

78. Mitchell, J.B., Chen, L., Langworthy, K., Fabrizio, K., and Boettcher, S.W. (2022). Catalytic proton–hydroxide recombination for forward-bias bipolar membranes. ACS Energy Lett. *7*, 3967–3973. https://doi.org/10.1021/acsenergylett.2c02043.

79. Wang, J., Zhao, Y., Setzler, B.P., Rojas-Carbonell, S., Ben Yehuda, C., Amel, A., Page, M., Wang, L., Hu, K., Shi, L., et al. (2019). Poly(aryl piperidinium) membranes and ionomers for hydroxide exchange membrane fuel cells. Nat. Energy *4*, 392–398. https://doi.org/10.1038/s41560-019-0372-8.

80. Cooper, K.R. (2010). Progress toward accurate through-plane ion transport resistance measurement of thin solid electrolytes. J. Electrochem. Soc. *157*, B1731. https://doi.org/10.1149/1.3481561.

81. Germer, W., Harms, C., Tullius, V., Leppin, J., and Dyck, A. (2015). Comparison of conductivity measurement systems using the example of nafion and anion exchange membrane. Solid State Ionics *275*, 71–74. https://doi.org/10.1016/j.ssi.2015.02.023.

82. Murbach, M.D., and Schwartz, D.T. (2019). Open software and datasets for the analysis of electrochemical impedance spectra. Electrochem. Soc. Interface *28*, 51–54. https://doi.org/10.1149/2.F05191if.

83. Murbach, M.D., Gerwe, B., Dawson-Elli, N., and Tsui, L.-k. (2020). impedance.py: a python package for electrochemical impedance analysis. J. Open Source Softw. *5*, 2349. https://doi.org/10.21105/joss.02349.